Comparison of vibration mitigation controllers for adaptive optics systems

Andres Guesalaga,[1,*] Benoit Neichel,[2] Francois Rigaut,[2] James Osborn,[1] and Dani Guzman[1]

[1]Pontificia Universidad Católica de Chile, 4860 Vicuna Mackenna, Casilla 7820436, Santiago, Chile

[2]Gemini Observatory Southern Operations Center, Colina el Pino s/n, Casilla 603, La Serena, Chile

*Corresponding author: aguesala@ing.puc.cl

Received 1 March 2012; revised 4 May 2012; accepted 21 May 2012; posted 22 May 2012 (Doc. ID 164027); published 29 June 2012

Vibrations are detrimental to the performance of modern adaptive optics (AO) systems. In this paper, we describe new methods tested to mitigate the vibrations encountered in some of the instruments of the Gemini South telescope. By implementing a spectral analysis of the slope measurements from several wavefront sensors and an imager, we can determine the frequencies and magnitude of these vibrations. We found a persistent vibration at 55 Hz with others occurring occasionally at 14 and 100 Hz. Two types of AO controllers were designed and implemented, Kalman and H_∞, in the multiconjugate AO tip–tilt loop. The first results show a similar performance for these advanced controllers and a clear improvement in vibration rejection and overall performance over the classical integrator scheme. It is shown that the reduction in the standard deviation of the residual slopes (as measured by wavefront sensors) is highly dependent on turbulence, wind speed, and vibration conditions, ranging—in terms of slopes RMS value—from an almost negligible reduction for high speed wind to a factor of 5 for a combination of low wind and strong vibrations. © 2012 Optical Society of America

OCIS codes: 010.1080, 120.7280.

1. Introduction

Adaptive optics (AO) is a sophisticated technology that has been successfully implemented to reduce the degrading effects of the Earth's atmosphere on optical astronomical imaging. Nowadays, almost all large telescopes are equipped with AO, and all the future extremely large telescopes are based on this technology. As AO systems become better at correcting the atmospheric turbulence, other factors such as vibrations in the instruments and the telescope itself become increasingly important to gain the next step in performance. This is especially true for exoplanet AO systems where the residual wavefront error is very low, but it might also impact significantly the performance of other AO systems [1–5].

Vibrations can be caused by many different situations, such as wind shaking of the telescope structure, mechanical components in the instruments (e.g., fans, cryo-cooler and motors), or even telescope tracking errors. Identifying the source of the vibration can be difficult, and usually requires extensive measurements and specific equipment such as accelerometers or dedicated wavefront sensors (WFS). Moreover, mechanical damping is not always possible. In that case, recent studies suggested the use of control techniques needed to enhance AO performance in the presence of vibrations [6]. As an AO system can correct for the turbulence, the same active devices can be used to compensate for other sources of perturbations. These techniques have been successfully implemented and tested at laboratory level [7] and recently started to be used on operational systems [8,9]. For the future Extremely Large Telescopes, advanced controllers are considered as the baseline for vibration rejection [8–11].

1559-128X/12/194520-16$15.00/0

In this paper, we describe the characterization of the vibrations and testing of different control techniques on the multiconjugate AO system (GeMS), installed at the Gemini South Observatory. The vibrations are characterized by a spectral analysis of the GeMS WFS and Gemini South AO Imager (GSAOI) images. We then use this data to artificially induce similar vibrations with a tip–tilt mirror (TTM) and simulate atmospheric turbulence on the GeMS optical bench. This allows us to run several control algorithms in a controlled environment, and test them in a few different scenarios. Our approach was to define a set of controllers and test them against different ranges of inputs, assessing their performance and robustness. Three control laws have been implemented: the classic integrator, linear quadratic Gaussian (LQG) (based on a Kalman estimator) [12,13], and H_2/H_∞ [14–16] synthesis methods. While most of the recent research effort to cope with vibrations has been concentrated on LQG control laws, here we also propose and test the H_∞ synthesis method as an alternative.

In Section 2 we describe the GeMS instrument and present the characterization of the vibrations. In Section 3 we describe the theory behind each of the controllers implemented here. In Section 4 we analyze the impact of Bode's theorem on the closed-loop performance, Section 5 presents the results from four test cases, and Section 6 discusses stability and robustness of the controller. Finally in Section 7, conclusions are stated and some ideas for further work are given.

2. Vibration Characterization for GeMS

In this section, we characterize the vibration environment seen by GeMS. Our goal here is not to provide a fine analysis of the vibration environment, but rather to draw general trends to later illustrate the performance of different controllers for realistic examples.

A. Introduction to GeMS

GeMS is the Gemini multiconjugate AO system. A schematic view of the main components is shown in Fig. 1.

GeMS uses 5 artificial Laser Guide Stars (LGS) with their associated LGS WFS (LGSWFS) and three deformable mirrors (DM) to compensate the turbulence over a field of view of 2 arcmin. Besides this, three Natural Guide Stars (NGSs) are required for the control of the tip–tilt and plate scale modes. The NGS consists of three probes, each containing a reflective pyramid that acts like a quad-cell feeding a set of four fibers and associated avalanche photodiodes.

Three NGS WFS(NGSWFS) provide six X-Y slopes necessary to generate global tip and tilt residuals that feed a TTM controller residing in the real-time controller (RTC). Plate scale modes can also be estimated from this set of slopes [17], but they are not considered in this paper. The laser loop and the NGS loop can be driven independently at a rate of up to 800 Hz.

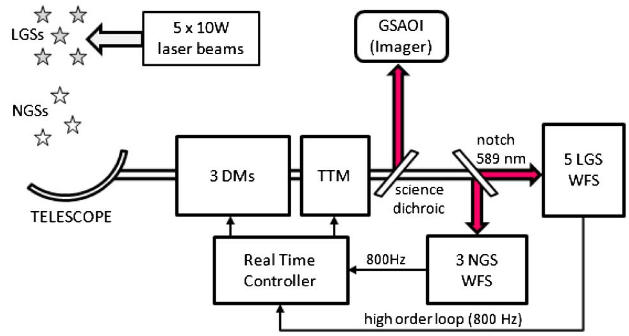

Fig. 1. (Color online) GeMS.

GeMS delivers a uniform, diffraction-limited corrected near-infrared image to GSAOI, which can read up to four windows providing tip–tilt information of NGS at a rate of 800 Hz. These tip–tilt values can be used to control the TTM, or to monitor the performance at the science detector level. In the following, we use them to measure the amount of vibrations seen by the science detector, which is what one wants to compensate for.

The optical bench also includes calibration sources that can generate artificial stars (either laser or natural guide stars) that have been extensively used in this work. In conjunction with these calibration sources, the DM and the TTM can be used to generate perturbations to simulate turbulence or vibrations.

More details about GeMS can be found in other papers [18,19].

B. Vibration Characterization for GeMS

GeMS started on-sky commissioning in January 2011, and it has been at the telescope for the first five months of 2011. During all this commissioning period, we have gathered data to characterize the vibration environment seen by GeMS. Vibrations were measured on three distinctive paths highlighted in Fig. 1. More specifically, we have used

- calibration sources data from NGSWFS, LGSWFS and GSAOI,
- on-sky data from NGSWFS and LGSWFS in open and closed-loop.

In the following, we make use of these data to specify typical perturbations seen by GeMS. Our objective is to construct a set of realistic perturbations (turbulence and vibrations) at GeMS's input, to later artificially reproduce them in a controlled way using the TTM and simulating atmospheric turbulence on the GeMS optical bench.

1. *Calibration Sources Data*

Data acquired with the calibration sources are not affected by the turbulence, and can be used to easily identify the vibrations. They also benefit from a much higher signal-to-noise ratio than on-sky data.

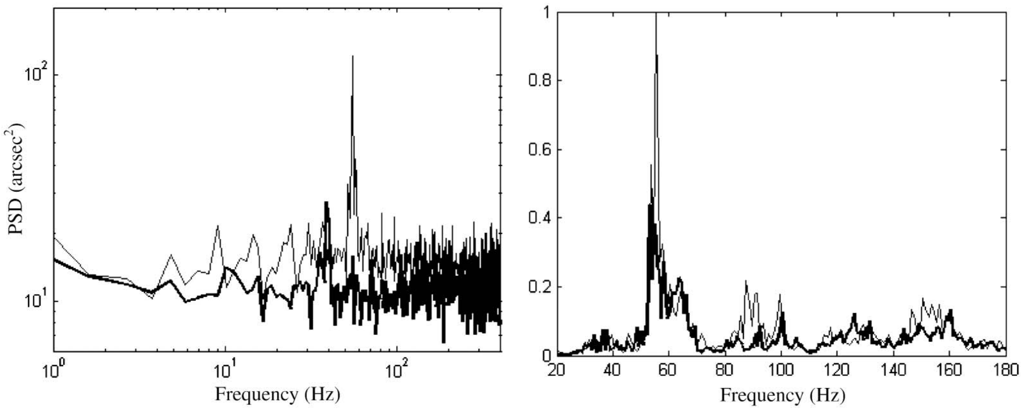

Fig. 2. Data from calibration sources. Left panel: PSDs for NGSWFS (tip or X is coarse line and Tilt or Y is fine line). Right panel: LGSWFS (fine line) and GSAOI-tip/tilt (coarse line). The plots on the right panel are in a PSD × frequency representation to emphasize the distribution of energy.

Moreover, the comparison of the data coming from the different WFS and GSAOI tip–tilt data allows separating what is in the common path or noncommon path. This is an important step, as the design of the controller will depend on this. Measurements are open loop (OL), but with the DM flattened to ensure a good spot quality.

Plots in Fig. 2 (left) show an example of the power spectra density (PSD) acquired with the NGSWFS (tip or X is coarse line and tilt or Y is fine). The main feature that appears on these PSDs is a strong vibration peak around 55 Hz for the Y axis. We have identified that the cryo-coolers of GSAOI were producing this vibration. In Fig. 2 (right), we show the PSD of the Y axis as measured by the LGSWFS (fine line), and the spot motion on the GSAOI windows (coarse line). These plots are in a PSD × frequency representation, in order to emphasize the distribution of the energy among the different contributors.

These plots confirm that the 55 Hz vibration is seen by all the WFS and the science camera as well, so it is a common path feature. We measure the amplitude of this vibration to be of the order of 5 to 10 mas rms, which would reduce the Strehl by approximately 10% in the H band.

2. *On-Sky Data*

Data acquired on the calibration sources are informative, but should be complemented by data acquired on-sky. Firstly, because some of the vibrations observed could be introduced by the calibration sources themselves, as seen for instance in Altair [5]. Secondly, because only on-sky data span the entire optical path and some vibrations can be introduced by optical elements that are located before the calibration sources. The main drawback of on-sky data is that they are affected by noise and turbulence, and it could be more difficult to disentangle the effect of vibrations.

For the NGSWFS, data were acquired while the LGS loop was closed in order to get smaller spots. We used either open-loop data or reconstructed open-loop data based on the combination of the residuals seen by the WFS and the commands sent to the TTM. The plots in Fig. 3 show two typical examples of open-loop PSDs measured at the NGSWFS level.

These plots clearly show that the 55 Hz peak can still be seen in the Y axis for on-sky data, which confirms that this vibration is not induced by the calibration unit itself. Interestingly, and on top of this 55 Hz peak, we also see some examples where an additional peak appears. In particular, we do see very sharp peaks at higher frequencies, as for instance above 100 Hz in Fig. 3 (left panel) and in Fig. 4 for LGSWFS. These vibrations may be introduced outside of the optical bench, as they are not seen on the calibration sources data. In addition, they may not always be present in the data, as for instance in Fig. 3, where they are detected in the April data, but not in the March data. In some examples (not illustrated here) we also see a broad peak around 14 Hz, which is believed to be induced by the top-end of the telescope, and the secondary mirror structure [5]. This peak is not always present and may be excited by wind-shake. These two plots also illustrate the range of variation that one can expect for the turbulence contribution. Indeed, depending on the turbulence strength (referred as seeing in the remainder of the paper) and wind speed conditions, the continuum of the spectrum will vary [20]. In addition, the noise level will also change significantly depending on the guiding star (GS) magnitudes, and some vibrations may be lost in noise. In the two examples chosen here, the GS magnitude was roughly the same.

The tip–tilt signal coming from the LGSWFS cannot be used directly, as the up-link tip–tilt of the laser is compensated by fast tip–tilt platforms in the laser projection system. We used LGSWFS data when the up-link and the NGSWFS loop were open. This may affect the amplitude of the vibration, as the linearity range of the LGSWFS is only of the order of a few arcseconds, but this should not affect the frequencies at which vibrations are detected. An example of PSD measured on-sky at the LGSWFS level is presented in Fig. 4 for the tilt direction. The 55 Hz peak is

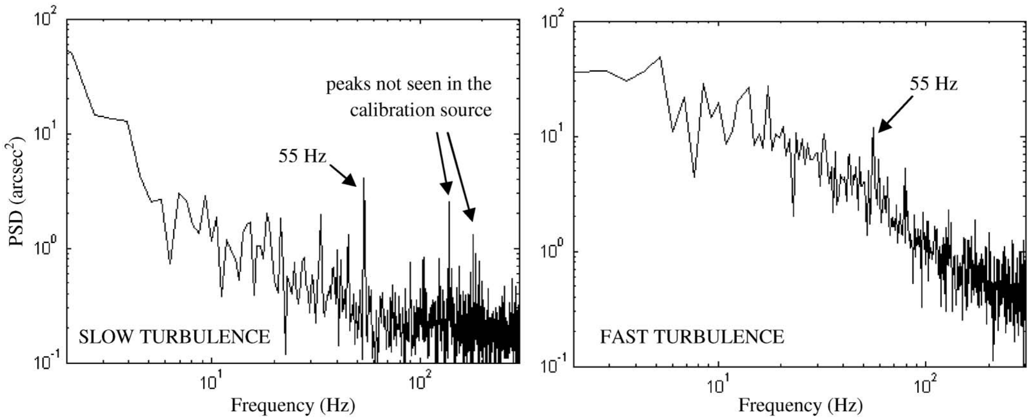

Fig. 3. On-sky PSDs for the NGSWFS (tilt). Left: data acquired in April 2011; right: data acquired in March 2011.

clearly detected, which confirms that this vibration lies in the common optical path. Some higher frequency sharp peaks are also seen, some of them not being detected by the NGSWFS, due to noise, laser uplink-related vibrations, or noncommon path effects. Note that this data set has not been taken simultaneously as the NGSWFS ones presented above, so the vibration contents may also evolve depending on the telescope configuration.

Finally, only few on-sky data have been recorded with the GSAOI windows so far, and only at a low frame rate. The first results seem to indicate the same trends as the one seen on the LGSWFS, confirming that these two paths are highly correlated.

3. *Results*

The previous analysis allowed us to identify a common path vibration at 55 Hz. This vibration is clearly and always identified on the entire optical path used in this study. This is not the case for other perturbations that are evolving with time and telescope configuration. For instance, we found that depending on the instrument suite mounted at the Cassegrain focus, or the telescope elevation, the vibration content evolves (see also [5]). In addition, the vibrations measured by a WFS may be evolving differently from what would be measured on the science path. Detailing all these data is out of the scope of this paper, and we rather want to stress that an analysis at the science level is primordial.

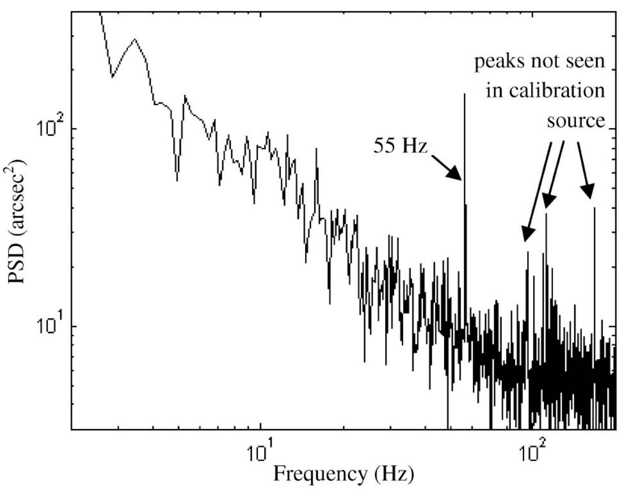

Fig. 4. On-sky PSDs for the LGSWFS. Data acquired in March 2011.

C. Simulated Conditions on the Bench

As described above, data collected on-sky can be very different from one night to another, depending on atmospheric and telescope conditions. In order to be able to compare different control algorithms in a reproducible way, we have chosen to generate typical vibrations and turbulence conditions on the bench by artificially exciting the TTM. Based on the on-sky data analysis, we have chosen to study the case of three vibrations peaks, respectively, at 14, 55, and 100 Hz. At first, each of these vibrations is introduced independently. These three vibrations are illustrative examples as they occur, respectively, within the loop bandwidth, in the overshoot of the closed loop, and at a frequency higher than the loop bandwidth. Different amplitudes for each vibration can be introduced as well. In addition, we chose to simulate two seeing conditions: a slow turbulence with a cut-off frequency around 15 Hz (slow seeing case), and a fast turbulence with a cut-off frequency around 100 Hz (fast seeing case). These two seeing cases and three vibration conditions will allow us to illustrate and compare the behavior of the different control algorithms for representative conditions seen by GeMS.

In Fig. 5 we show four examples of OL data simulated on the bench, as measured by the LGSWFS that we will use later in this paper. The plots are (i) slow seeing and 55 Hz vibration (left panel), (ii) fast seeing and 55 Hz vibration (continuous line, right panel), (iii) slow seeing and 14 Hz vibration (dashed line, right panel), and (iv) fast seeing and a 100 Hz vibration (dotted line, right panel).

3. Controller Theory

In the following, we will use a modeling of the AO closed loop as described in Fig. 6, where φ^{tur}, φ^{res},

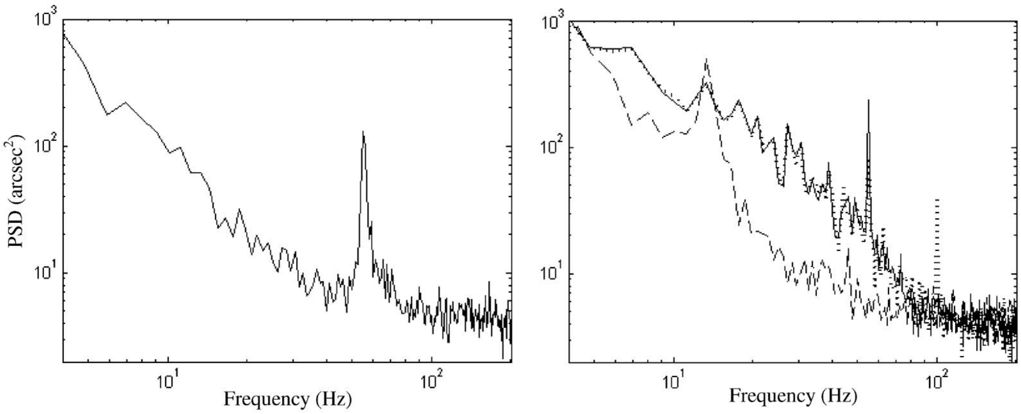

Fig. 5. OL data simulated on the bench as seen by the LGSWFS. Left panel: slow seeing and 55 Hz vibration. Right panel: fast seeing and 55 Hz vibration (continuous line), slow seeing and 14 Hz vibration (dashed line), fast seeing and a 100 Hz vibration (dotted line).

and φ^{cor} represent, respectively, the turbulence, residual, and correction phases. Input w is the measurement noise, y is the measurements, and u is the control voltages.

The residual phase is defined by the difference between the input turbulence and the correction phase: $\varphi^{\mathrm{res}} = \varphi^{\mathrm{tur}} - \varphi^{\mathrm{cor}}$. The model describing the WFS measurement process is assumed to be linear and can be defined by

$$y_n = D\varphi^{\mathrm{res}}_{n-1} + w_n, \tag{1}$$

where y_n is the vector containing the measured slopes at time n, D is the interaction matrix describing the linear relationship between the phase and measurement, and w_n is the white noise with covariance C_w.

From the controller's input standpoint, the actuator command u at time n generates a correction phase given by Nu_{n-1}, i.e., delayed by one frame. N is the so-called influence matrix that defines the relationship between voltages and correction phase.

Taking these notations into Fig. 6, yields to the following closed-loop diagram.

In our case, we assume that the turbulence is only the tip and tilt modes, and that these modes are decoupled from each other and from the higher-order modes. This allows us to carry out a single-input/single-output (SISO) analysis of the problem.

The goal of this section is to design three different controllers (i.e., the block G in Fig. 7) for a later implementation in GeMS. References are given in each case for a more detailed treatment of the algorithms and theories.

A. Integrator

The classical integrator is the most common controller in AO, and the current default tip–tilt controller in GeMS. The controller is defined by

$$G(z) = \frac{K_i}{1 - az^{-1}}, \tag{2}$$

where z is the Z-transform operator and a is generally unity, unless a controller free from winding-up is desired (i.e., a "leaky" integrator). Parameter K_i represents the gain of the loop and is adjusted according to noise and performance requirements. An optimal way to define this gain is proposed by Gendron and Lena [21].

B. Kalman

The Kalman approach (a special case of the LQG approach) provides an optimal correction criterion for the mirror commands (voltages) that minimize the variance of the slope residuals. The problem is split into a stochastic estimation problem and a deterministic control problem. The first step estimates the turbulence phase by minimizing a stochastic criterion (Kalman filter); the second finds the best commands for the TTM, assuming negligible dynamics, i.e., a static projection of the estimated state-space

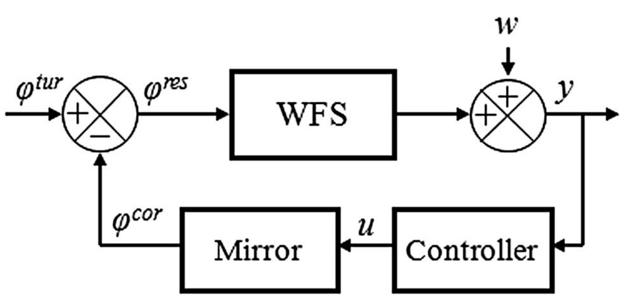

Fig. 6. Closed-loop model of the tip–tilt AO loop.

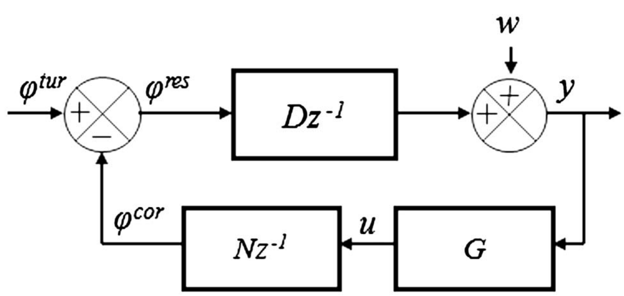

Fig. 7. AO closed-loop block diagram.

values onto the TTM modes [12]. An extension of the Kalman filter to AO loops for mirrors with dynamics is described in [22].

The optimal correction criterion is defined by

$$\begin{aligned}\min \langle |\varepsilon_{n+1}|^2 \rangle_{\varphi,\mathrm{noise}} &= \min \langle |\varphi_{n+1}^{\mathrm{tur}} - \varphi_{n+1}^{\mathrm{cor}}|^2 \rangle_{\varphi,\mathrm{noise}} \\ &= \min \langle |\varphi_{n+1}^{\mathrm{tur}} - Nu_n|^2 \rangle_{\varphi,\mathrm{noise}}. \quad (3)\end{aligned}$$

In words, this criterion minimizes the spatial variance of phase residuals at the telescope pupil over the turbulence and noise, assuming an orthonormalized base.

The Kalman approach requires a modeling of the disturbances entering the AO loop. This can be simplified by considering two type of perturbations: a turbulent signal φ_n^{tur}, and several vibration signals $\varphi_n^{\mathrm{vib},i}$. Hence, the total disturbance is

$$\varphi_n = \varphi_n^{\mathrm{tur}} + \varphi_n^{\mathrm{vib},1} + \varphi_n^{\mathrm{vib},2} + \ldots + \varphi_n^{\mathrm{vib},i}. \quad (4)$$

In previous reports [7,22], the vibration component $\varphi_n^{\mathrm{vib},i}$ is a discrete version of a continuous mechanical oscillatory signal, characterized by its damping coefficient and natural frequency. This leads to an auto-regressive second-order (AR2) model [22],

$$\varphi_{n+1}^{\mathrm{vib},i} = a_1^{\mathrm{vib},i}\varphi_n^{\mathrm{vib},i} + a_2^{\mathrm{vib},i}\varphi_{n-1}^{\mathrm{vib},i} + v_n^{\mathrm{vib},i}, \quad (5)$$

where a_1 and a_2 are the AR2 coefficients and $v_n^{\mathrm{vib},i}$ is the white noise. This second-order model can also be used to represent a linear simplification of nonresonating disturbances such as atmospheric turbulence by choosing a_1 and a_2 such that the damping factor is larger than unity. The turbulence can be modeled by

$$\varphi_{n+1}^{\mathrm{tur}} = a_1^{\mathrm{tur}}\varphi_n^{\mathrm{tur}} + a_2^{\mathrm{tur}}\varphi_{n-1}^{\mathrm{tur}} + v_n^{\mathrm{tur}}, \quad (6)$$

by defining the state-vector:

$$x_n = \begin{bmatrix} \varphi_n^{\mathrm{tur}} \\ \varphi_{n-1}^{\mathrm{tur}} \\ \varphi_n^{\mathrm{vib}} \\ \varphi_{n-1}^{\mathrm{vib}} \end{bmatrix}. \quad (7)$$

The process described by Eqs. (4), (6), and (7) can be reformulated as a linear time invariant state-space model representing the combination of a turbulence plus a single vibration signal,

$$x_{n+1} = Ax_n + v_n y_n = Cx_n - DNu_{n-2} + w_n, \quad (8)$$

with the following expanded representation:

$$\underbrace{\begin{bmatrix} \varphi_{n+1}^{\mathrm{tur}} \\ \varphi_n^{\mathrm{tur}} \\ \varphi_{n+1}^{\mathrm{vib}} \\ \varphi_n^{\mathrm{vib}} \end{bmatrix}}_{x_{n+1}} = \underbrace{\begin{bmatrix} a_1^{\mathrm{tur}} & a_2^{\mathrm{tur}} & 0 & 0 \\ 1 & 0 & 0 & 0 \\ 0 & 0 & a_1^{\mathrm{vib}} & a_2^{\mathrm{vib}} \\ 0 & 0 & 1 & 0 \end{bmatrix}}_{A} \underbrace{\begin{bmatrix} \varphi_n^{\mathrm{tur}} \\ \varphi_{n-1}^{\mathrm{tur}} \\ \varphi_n^{\mathrm{vib}} \\ \varphi_{n-1}^{\mathrm{vib}} \end{bmatrix}}_{x_n} + \underbrace{\begin{bmatrix} v_n^{\mathrm{tur}} \\ 0 \\ v_n^{\mathrm{vib}} \\ 0 \end{bmatrix}}_{v_n}, \quad (9)$$

$$y_n = \underbrace{[0 \quad D \quad 0 \quad D]}_{C} x_n - DNu_{n-2} + w_n. \quad (10)$$

It has been shown [6,12] that for this system, the optimal controller (in terms of residual phase variance) is a LQG controller consisting in a Kalman filter and a reconstructed state feedback with the following equations,

$$\begin{aligned}\hat{x}_{n/n} &= A\hat{x}_{n/n-1} + L(y_n - C\hat{x}_{n/n-1} + DNu_{n-2}), \\ \hat{x}_{n+1/n} &= A\hat{x}_{n/n}, \\ u_n &= -K\hat{x}_{n+1/n}, \quad (11)\end{aligned}$$

where $K = -N^{-1}[1 \quad 0 \quad 1 \quad 0]$, and $L = \sum_\infty C^T (C\sum_\infty C^T + \sigma_w^2)^{-1}$, where Σ_∞ is the static solution of a Ricatti equation and σ_w^2 is the standard deviation of the measurement noise. Using the z-transform of these equations, we compute the LQG controller transfer function:

$$G(z) = -K[I_d - (I_d - LC)Az^{-1} + LDKz^{-2}]^{-1}L. \quad (12)$$

Application cases of this approach can be found in [7,8,11,23].

C. H_∞ Control

Looking for new contributions to this challenging control problem, we suggest the use of frequency-based design techniques. These syntheses techniques, based on the minimization of H_2 and H_∞ norms [14,16], are particularly suitable to tackle vibration rejection problems, since they can readily take TTM loop dynamics and performance requirements into account during the design stages.

1. H_∞ Theory

H_∞ methods are used to synthesize controllers looking for a robust performance of the closed-loop. Here, the control problem is presented as a mathematical optimization problem, and then the synthesis technique finds it.

A continuous-time representation is required in these techniques, so a Laplace representation is used in the problem formulation.

Plant $P(s)$ has two inputs, the exogenous input r, which includes reference signal and disturbances, and the manipulated variables u. There are two outputs: the signals contained in vector z that we want to minimize, and the error e, which we use to control the system. The input e is used by $G(s)$ to calculate the manipulated variable u. In matrix form, the system is

$$\begin{bmatrix} z \\ e \end{bmatrix} = P(s)\begin{bmatrix} r \\ u \end{bmatrix} = \begin{bmatrix} P_{11}(s) & P_{12}(s) \\ P_{21}(s) & P_{22}(s) \end{bmatrix}\begin{bmatrix} r \\ u \end{bmatrix}, \tag{13}$$

$$u = G(s)e. \tag{14}$$

Dropping the Laplace operator s for simplicity, the output z can now be expressed in terms of the input r by

$$z = F_l(P, G)r. \tag{15}$$

From Eq. (14) and the loop configuration in Fig. 8, F_l can be represented by

$$F_l(P, G) = P_{11} + P_{12}G(I - P_{22}G)^{-1}P_{21}. \tag{16}$$

The H_∞ synthesis finds a controller G such that the H_∞ norm of $F_l(P, G)$ is minimized. An equivalent definition exists for the H_2 synthesis method.

The infinity norm of $F_l(P, G)$ is defined as

$$\|F_l(P, G)\|_\infty = \sup_\omega \bar{\sigma}(F_l(P, G)(j\omega)), \tag{17}$$

where $\bar{\sigma}$ is the maximum singular value of the matrix $F_l(P, G)(j\omega)$.

Doyle *et al.* [14] demonstrate that the computation for H_2 (reminiscent of the classical LQG problem) and the H_∞ solutions follow the same path, which basically consists in solving two Ricatti equations in their static form (optimal estimation and optimal control problems). They also show that one can switch from one solution to the other by simply modifying a single parameter in the algorithm. No significant differences should be expected from using either of them; however, since the H_∞ norm corresponds to the highest value (worst case) of the spectrum to be minimized, it can be more appropriate in cases where resonances or vibrations exist.

The term H_∞ comes from the name of the space over which the optimization is pursued, i.e., the space of matrix-valued functions that are analytic and bounded in the open right-half of the complex plane defined by $\mathrm{Re}(s) > 0$. The H_∞ norm is the maximum singular value of the function over that space, and it can be interpreted as the maximum gain in any direction of the matrix-valued functions and at any frequency. For single-input/single output systems, this is the maximum magnitude of the frequency response. H_∞ techniques can be used to minimize the closed-loop impact of a perturbation.

The algorithms that synthesize the optimal controller require that the standard configuration be represented in a state-space form, so system $P(s)$ is be represented in a compact state-space form:

$$P[A, B_1, B_2, C_1, C_2, D_{11}, D_{12}, D_{21}, D_{22}] : \times \begin{bmatrix} A & B_1 & B_2 \\ C_1 & D_{11} & D_{12} \\ C_2 & D_{21} & D_{22} \end{bmatrix}, \tag{18}$$

where every element in P is a combination of the state-space matrix A and the corresponding vectors. For instance, $P_{21}(s) = C_2(sI - A)^{-1}B_1 + D_{21}$.

The state-space form of the controller $G(s)$ is obtained from [14]:

$$\begin{aligned} A_K &= A + \gamma^{-2}B_1B_1'X_\infty - B_2B_2'X_\infty \\ &\quad - (I - \gamma^{-2}X_\infty Y_\infty)^{-1}Y_\infty C_2'C_2, \\ B_K &= B_2'X_\infty, \\ C_K &= (I - \gamma^{-2}X_\infty Y_\infty)^{-1}Y_\infty C_2', \\ D_K &= 0, \end{aligned} \tag{19}$$

where X_∞ and Y_∞ are the solutions of two Ricatti equations given by

$$X_\infty = \mathrm{Ric}\begin{bmatrix} A & \gamma^{-2}B_1B_1' - B_2B_2' \\ B_1B_1' & -A \end{bmatrix}, \tag{20}$$

$$Y_\infty = \mathrm{Ric}\begin{bmatrix} A' & \gamma^{-2}C_1C_1' - C_2C_2' \\ -B_1B_1' & -A \end{bmatrix}. \tag{21}$$

Doyle and co-authors define γ such that $\|F_l(P, G)\|_\infty < \gamma$. No explicit solution exists for γ, so it must be found by an iterative search method to get a value as close as desired to the minimum achievable infinity norm for F_l.

2. *Application of H_∞ to the Tip–Tilt Problem*

In this frequency approach, the problem is stated as the servo-control system in Fig. 9.

The setpoint r is the incident tip or tilt, and e is the residual out of the mirror, which is measured (noise added) and later multiplied by controller $G(s)$ to generate the manipulated variable to move the TTM

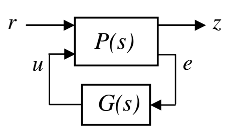

Fig. 8. Standard controller-plant configuration for H_∞/H_2 synthesis.

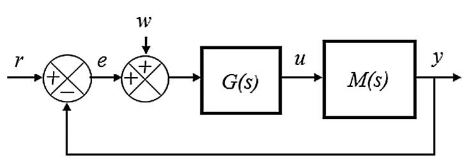

Fig. 9. Servo-control problem.

whose output is subtracted to the tip or tilt of the incoming turbulence. The mirror transfer function $M(s)$ contains the dynamics of the actuators and the two-frame delay of a standard Shack–Hartmann AO loop.

The controller $G(s)$ is synthesized to reduce what is called the mixed-sensitivity norm [15]. This norm is formed as a weighted combination of the error transfer function or sensitivity function (SF), the control sensitivity function (CSF) associated to control energy usage, and the noise transfer function (NTF). From Fig. 9, these functions are defined by

$$\mathrm{SF}(s) = \frac{e(s)}{r(s)} = \frac{1}{1 + M(s)G(s)}, \tag{22}$$

$$\mathrm{CSF}(s) = \frac{u(s)}{r(s)} = \frac{G(s)}{1 + M(s)G(s)}, \tag{23}$$

$$\mathrm{NTF}(s) = \frac{e(s)}{w(s)} = \frac{-M(s)G(s)}{1 + M(s)G(s)}. \tag{24}$$

Contrary to the Kalman approach, we use the CSF instead of the NTF. The reason for this is that this function not only can be used to restrict the intensity of actuator signals, but it can also avoid excessive noise amplification by weighting the CSF at higher frequencies.

The closed-loop system in Fig. 9 is rearranged to form what is called the augmented representation shown in Fig. 10. Here, two weighting functions are added to the outputs to be minimized. Function $W_e(s)$ penalizes control errors (residuals) and $W_u(s)$ weights the actuator signal, so it restricts its usage at some frequencies. The latter can be used to attenuate the effect of noise amplification in the loop, i.e., a controller with a low-pass characteristic. These weighting functions are normally complementary, so that the contradictory requirements that good accuracy and control effort impose on the design can be met by the resulting controller.

From the general structure in Fig. 7 and the arrangement of Fig. 10,

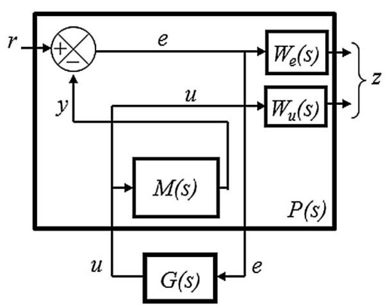

Fig. 10. Augmented representation used to synthesize the H_∞ controller, $G(s)$.

$$P(s) = \begin{bmatrix} P_{11}(s) & P_{12}(s) \\ P_{21}(s) & P_{22}(s) \end{bmatrix} = \begin{bmatrix} W_e(s) & -W_e(s)M(s) \\ 0 & W_u(s) \\ 1 & -M(s) \end{bmatrix}. \tag{25}$$

The controller $G(s)$ is derived from the minimization of the H_∞ norm in Eq. (18), given by

$$\min_G \|F_l(P,G)\|_\infty = \min_G \left\| \begin{matrix} W_e \cdot \mathrm{SF} \\ W_u \cdot \mathrm{CSF} \end{matrix} \right\|_\infty. \tag{26}$$

For implementation in the RTC, $G(s)$ is digitized using zero-order-hold transformations.

In the previous Kalman approach, the disturbances are modeled to account for turbulence and vibration spectral amplitude. Here, they are assumed to have a flat spectrum, and the information on the turbulence and vibration amplitude is contained in the $W_e(s)$ function used during the controller synthesis so that each frequency is weighted according to its intensity. This will become apparent in the next section. Another feature of this design approach is that it can also include physical limitations of the actuators (dynamic and static) via the function $W_u(s)$.

3. *Design Example Using H_∞ Control*

A simple design case is described for the H_∞ method. Open-loop tip–tilt slopes were collected from NGS WFSs, in the case of slow seeing and strong 55 Hz vibration (Fig. 11). In order to tackle both the turbulence and the vibration, W_e is fitted to the standard deviation of slopes using rational functions [see Eq. (27)]. Function W_e weighs the error signal at low frequencies and also at a specific vibration frequency:

$$W_e(s) = \frac{C_0}{s + C_1} \cdot \frac{s^2 + 2\eta_1\omega_o s + \omega_o^2}{s^2 + 2\eta_2\omega_o s + \omega_o^2}, \tag{27}$$

where s is the Laplace operator and parameters C_0 and C_1 are determined by the turbulence (lower part

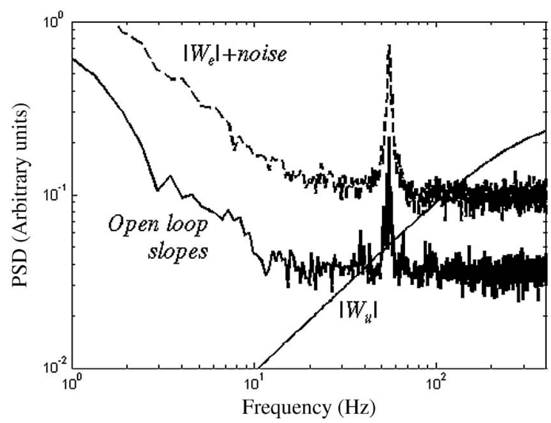

Fig. 11. Fitting of W_e to open-loop NGSWFS data and definition of W_u according to manufacturer's specs (W_e plot has been vertically displaced for clarity). Data are taken from observations on Feb. 11, 2011.

of the spectrum). In turn, ω_o corresponds to the vibration frequency and the damping factors η_1 and η_2 define the height and width of the vibration peak.

The mirror transfer function, $M(s)$, contains the dynamics of the actuators and the two-frame delay of the standard Shack–Hartmann loop. According to the manufacturer, the bandwidth of the mirror actuators is 380 Hz. A value of 400 Hz was measured experimentally, so the mirror dynamics and loop delays were represented by the following transfer function:

$$M(s) = \frac{e^{-2\Delta s}}{0.0025s + 1}, \tag{28}$$

where Δ is the sensor sampling interval. This pure delay is later approximated to rational functions using bilinear transformations.

A dynamic representation of the mirror is also necessary when considering resonances of these devices [22]. The effect of neglecting these dynamics is discussed later in the paper for the Kalman technique. In the H_∞ synthesis approach, it is included by shaping the function W_u with a high-pass characteristic that penalizes the use of control signals above the TTM's cutoff frequency that also reduces the sensitivity of the controller to high frequency noise. Mathematically,

$$W_u(S) = C_2 \cdot \frac{S}{C_3 S + 1}, \tag{29}$$

Table 1. Parameters for W_e and W_u

Parameter	Value
C_0	15.3
C_1	5.1
η_1	0.4
η_2	0.02
ω_o	$2 \cdot \pi \cdot 55.5$ rad/s
C_2	$1.5 \cdot 10^{-3}$ s
C_3	$5 \cdot 10^{-4}$ s

where C_2 and C_3 are adjusted to represent the characteristic of the TTM bandwidth and noise. Figure 11 shows the result of fitting function W_e and noise to the data (the fitting is vertically displaced for clarity). We have found that function W_u can be further adjusted to generate an SF with acceptable overshoot and closed-loop bandwidth.

In this paper, a trial and error approach has been used for fitting W_e and W_u to the experimental data, and the resulting parameters are presented in Table 1. Further work is needed to find these parameters using identification techniques, as suggested in [8,11,23]. A fifth-order controller is obtained after the synthesis process described above, with Fig. 12 (left) showing the SF of the resulting closed-loop system. As previously observed by Dessenne *et al.* [24] and Meimon *et al.* [23], if a high signal-to-noise regime is assumed for the measurements, the squared SF is proportional to the inverse of the disturbance in Fig. 11. In other words, if W_u is negligible over most of the spectrum, then

$$|\mathrm{SF}|^2 \propto 1/W_e. \tag{30}$$

Figure 12 (right) shows a plot of the PSD of the residuals obtained for the closed-loop system. When the filter parameters have been identified properly, as in this sample case, the closed-loop residual response tends to be flat for both advanced controllers. This demonstrates that the vibration and the turbulence have been efficiently rejected. The flatness of the residuals could then be used as a diagnostic of the efficiency of the filter. A criterion on the actual loop residuals could be used to adjust the filter parameters. In the next section, the RMS value of these residuals will be used to compare the performances of the three different controllers.

4. Bode's Theorem

At this point, it is important to stress the fact that shaping the closed-loop response of the AO system is not an arbitrary process, but it is subject to Bode's theorem, which imposes a strong restriction on the SF function and hence on the performance.

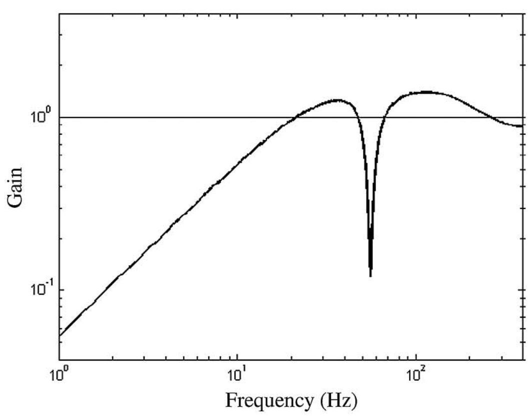

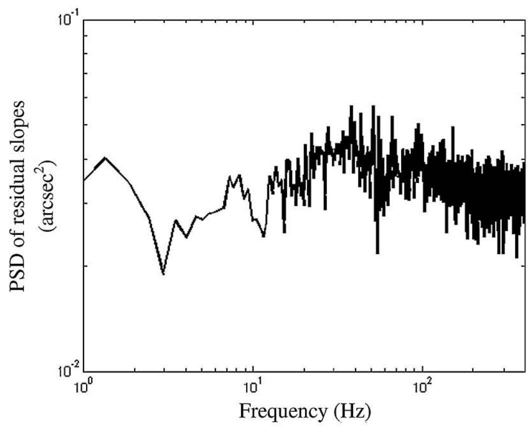

Fig. 12. SF obtained through H_∞ synthesis (left) and PSD of residuals obtained with the H_∞ controller (right).

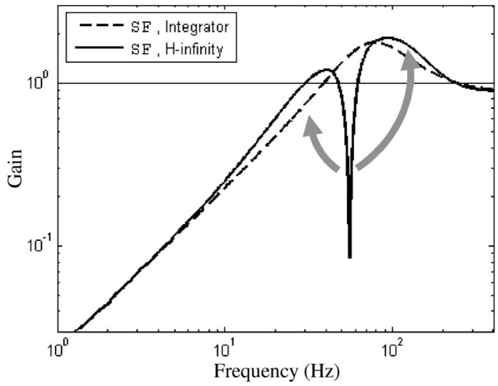

Fig. 13. Effect of vibration rejection due to Bode's theorem.

A discrete-time version of Bode's theorem [25] for a system with a sampling frequency f_s, states that

$$\int_{f \leq fs/2} \ln |\mathrm{SF}(f)| \mathrm{d}f = \beta, \quad (31)$$

where β is a constant depending only on the system to be controlled and not on the controller itself. This also implies that from the SF point of view, the mitigation of disturbances is fixed, so that the controller has to be shaped to reject those parts of the spectra where noise and disturbances are concentrated. Its performance should be assessed by looking at the loop residuals and not at the SF function. To clarify this limitation, Fig. 13 shows simulated SFs for a standard integrator and an H_∞ controller for the same OL slopes presented in Fig. 11. The latter has been synthesized to approach the integrator error rejection at low frequencies ($K_i = 0.4$) and also to reject a 55 Hz vibration. Clearly, the price to pay for the vibration rejection is a worsening in the error function around the notch.

5. Results

In this section, we define a set of controllers, designed for a given turbulence and vibration conditions, and we compare the performance of these controllers with respect to the classical integrator scheme when the input conditions are changing. The Kalman and H_∞ controllers described above have been implemented in GeMS' RTC, for notches at 14, 55, and 100 Hz. A sampling frequency of 800 Hz has been used throughout the experiments. In Fig. 14, we show their SF measured on noise, i.e., pure noise propagation function. A restricted frequency domain is shown only for better visualization.

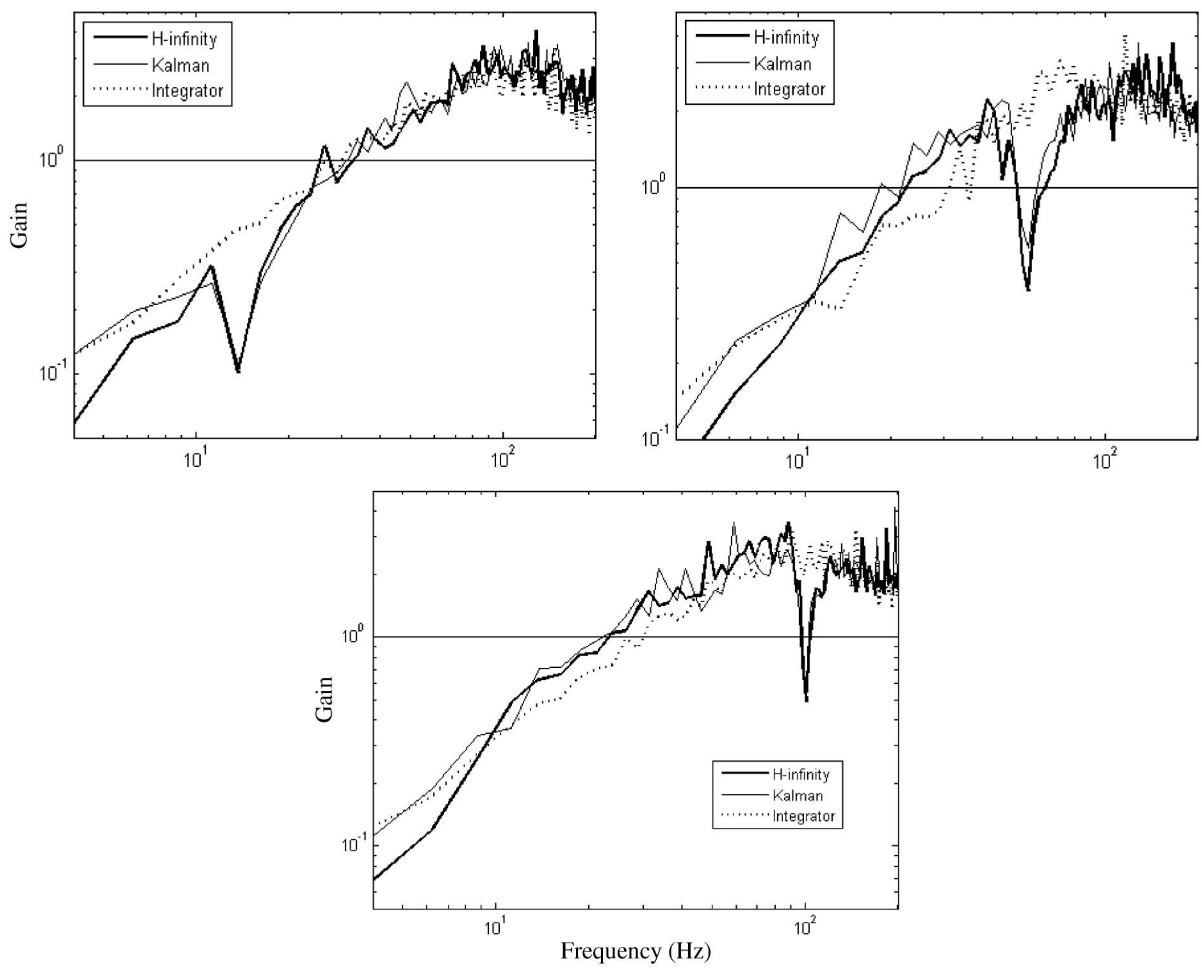

Fig. 14. SF for the three controllers in the case of a notch at 14 Hz (top-left), 55 Hz (top-right), and 100 Hz (bottom).

Note that, in order to make a fair comparison among controllers, they were finely tuned to get similar overshoots in the SF function (around 8 dB).

The controllers' performance was tested for three different types of turbulences:

- Case I: Wind speed matched to 1/SF and medium strength vibrations.
- Case II: Slow wind and strong vibrations.
- Case III: Fast wind and weak vibrations.

Vibrations were induced artificially in the loop by exciting the TTM as described in Subsection 2.C. GSAOI was not available for this experiment, and so the techniques were evaluated by measuring the standard deviation of slopes at the NGSWFS and LGSWFS. We use the LGSWFSs as a scoring camera for the performance of the three controllers, as if it would be our science path. The following analysis is carried out only for the tilt loop, since it is the direction where most of the disturbance appeared.

A. Case I: Wind Speed Matched to 1/SF and Medium Strength Vibrations

This case analyzes the performance of the closed-loop system when the actual turbulence matches the disturbance model assumed during the design of Kalman and H_∞ controllers (i.e., 1/SF). Figure 15 shows the PSD for OL, integrator, Kalman, and H_∞ for a vibration frequency of 14, 55, and 100 Hz, respectively. Notice the deterioration in the Kalman effectiveness to reject the 55 and 100 Hz vibrations (right panels), due to the omission of the TTM dynamics in the model, which become important at higher frequencies.

Table 2 summarizes the standard deviation of slope residuals at the LGSWFS and NGSWFS. The Kalman and H_∞ controllers reject the disturbance effectively, and closed-loop residuals are flat. For the 14 Hz vibration, the integrator can reduce partially the vibration, but for the 55 Hz and 100 Hz, it makes the situation worse due to an SF gain higher than 1 at such frequencies. This is where the advanced controller can provide most of the benefit. It is interesting to emphasize that the Kalman or H_∞ can be shaped to control frequencies that are outside of the closed-loop bandwidth. For these cases, the control works similarly to an OL scheme.

For these specific cases, improvement in performance brought by Kalman and H_∞ are of the order of 20%. Due to Bode's theorem, the advanced controllers are providing better rejection on the vibrations, but for medium and low frequencies, the performance is worse than the integrator; i.e., the attenuation of SF in one frequency band is compensated by a loss

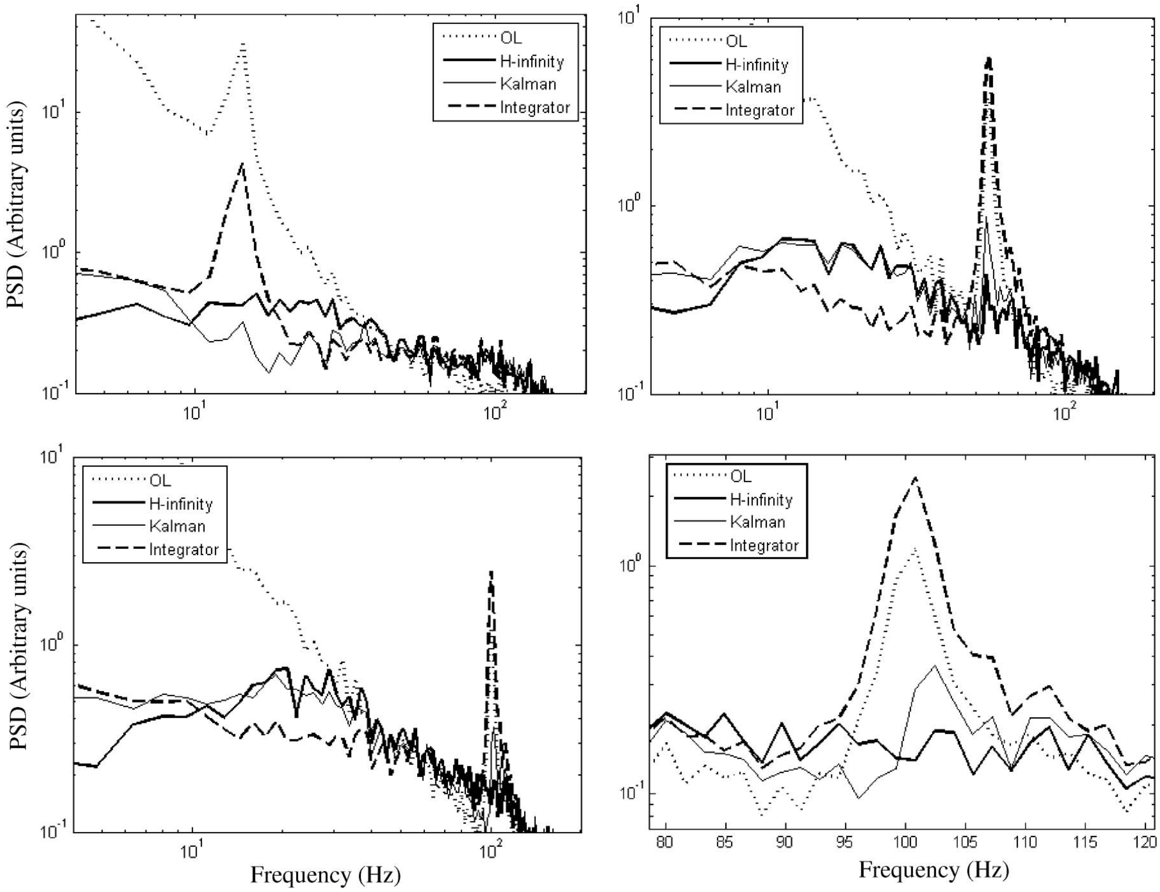

Fig. 15. Case I, 14 Hz vibration (top-left), 55 Hz (top-right), and 100 Hz (bottom-left): SF for OL, integrator, Kalman, and H_∞ controllers. The bottom-right shows a zoom around the 100 Hz, where Kalman starts underperforming due to the absence of the TTM dynamics in the design stage. A similar pattern is also observed for the 55 Hz vibration.

Table 2. RMS of Residual Slopes (Normalized to the Integrator Residual Variance)[a]

	14 Hz				55 Hz				100 Hz	
	I	I	II	III	I	I	II	III	I	I
Controller	NGS	LGS			NGS	LGS			NGS	LGS
Open-loop	5.25	5.63	22.63	2.39	5.29	5.83	3.89	2.32	6.69	6.82
Integrator	1.0	1.0	1.0	1.0	1.0	1.0	1.0	1.0	1.0	1.0
Kalman	0.88	0.88	0.63	0.9	0.83	0.83	0.31	1.0	0.94	0.88
H_∞	0.88	0.88	0.63	1.0	0.78	0.83	0.23	0.97	0.94	0.88

[a]LGS data and 100 Hz vibration data only show for case I.

in another frequency range. This tells us that the advantage of the advanced controllers is that they reject disturbances where their effect is strongest.

In summary, for a case where the filter perfectly matches the perturbation, significant improvements in performance can be achieved by advanced controllers compared to the classical integrator. We also measure that similar improvements in performance are obtained for Kalman and H_∞ controllers, and vibrations are effectively rejected in both cases.

B. Case II: Slow Wind and Strong Vibrations

Using the same controllers, we now modify the inputs for a slower turbulence and higher amplitude vibrations. Results are presented in Fig. 16. Note that spurious peaks are observed in the resulting plots at higher frequencies. These are caused by the third and 11th harmonics caused by excitation vibrations that surpass the maximum span of TTM actuators, generating saturated responses.

Kalman and H_∞ controllers are particularly well suited for this type of disturbance, since the turbulence spectrum is far from the loop bandwidth, so they can be easily rejected. Any improvement in vibration rejection will have a much higher impact on the overall performance; i.e., advanced controllers will outperform the integrator by a large factor. This is confirmed in Table 2, where the residuals generated by Kalman and H_∞ controllers are reduced by a factor of 3 to 5 when compared to those of the integrator.

The mismatch between the real turbulence and those assumed for the synthesis process generate a response where the vibrations are only partially eliminated. This tells us that there is still room for improvement and the design of deeper notch filters would reject the vibration even further: the trade-off between turbulence and vibration rejection is not optimal, as the filters have been designed for a different input.

C. Case III: Fast Wind and Weak Vibrations

In this third case, we introduce a faster turbulence, and we reduce the amplitude of the vibrations. This case represents the worst possible condition for the advanced controllers, i.e., a turbulence with frequency components similar to or higher than the loop cutoff frequency. Unfortunately, the higher SF gains at middle frequencies erase any possible improvement obtained by rejecting these vibrations; i.e., due to Bode's theorem, the integrator controller tends to have lower SF gains at these middle frequencies. As shown in Fig. 17 and Table 2 for the 55 Hz vibration, the residuals are higher than in the previous cases for all controllers, with no significant differences among them. Furthermore, as seen in the plots of Fig. 17, the vibration has been overcompensated, with a rejection that was too high compared to the

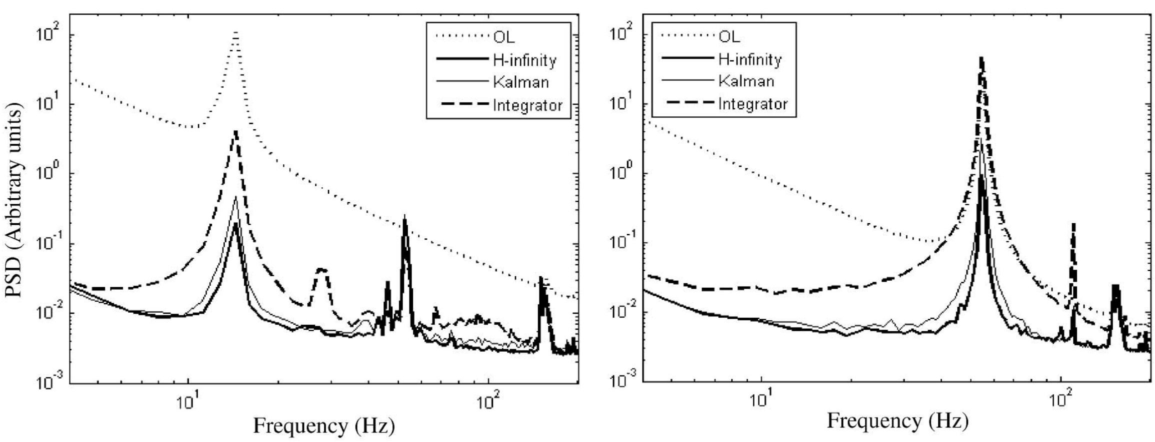

Fig. 16. Case II: PSD plots for OL, integrator, Kalman, and H_∞ controllers. Turbulence with 14 Hz vibration (left) and 55 Hz vibration (right). Third and 11th harmonics are observed due to TTM saturation.

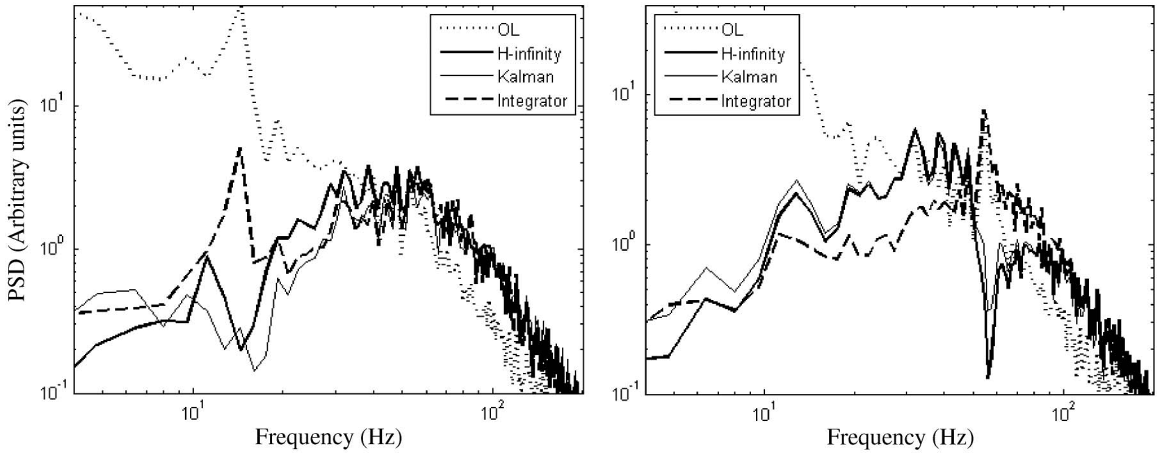

Fig. 17. Case III: PSD plots for vibrations at 14 Hz (left) and 55 Hz (right) for OL, integrator, Kalman and H_∞ controllers.

vibration amplitude. This over-rejection could have been used to better reject the turbulence at lower frequencies. However, it is worth noting that for this case and even though the filters are not optimal, advanced controllers are not getting worse results than the classical integrator. Hence, even in the presence of strong model errors, advanced controllers are still providing acceptable performance.

D. More Complex Disturbances

In this section, we study the possibility to handle more than one vibration at a time, or different kinds of perturbation. One of the amenities of frequency-based synthesis is that complex disturbance shapes can be easily defined using simple rational functions that describe the turbulence and vibrations without the need to change their model structure. This can be useful if an automated identification approach is pursued. Figure 18 shows the results of two further examples of more complex controllers: a two-vibration case (14 and 55 Hz) and a wide band disturbance (10–20 Hz). The left panel in Fig. 18 corresponds to the model identified for the disturbances in each case, and the right panel shows the resulting SF where the inverse proportionality with respect to the disturbance is apparent.

6. Discussions

Results presented above show significant gains for Kalman and H_∞ controllers, over a standard integrator, when turbulence is weak or when the disturbance is proportional to the inverse of the controllers' SF. For faster turbulence (higher wind speeds), this advantage vanishes, mainly due to the closed-loop bandwidth.

The results obtained in cases II and III demonstrate that matching the vibration and turbulence accurately is essential for a good performance of the Kalman and H_∞ controllers. By correctly identifying the turbulence frequency spectrum, better rejection of vibrations can be expected.

The approach of a controller design based on an offline identification and the subsequent design can provide substantial performance improvements for disturbances with stable behavior. This is the case for the 55 Hz vibration peak we analyzed above, which showed to be a weak function of telescope elevation or instrument orientation.

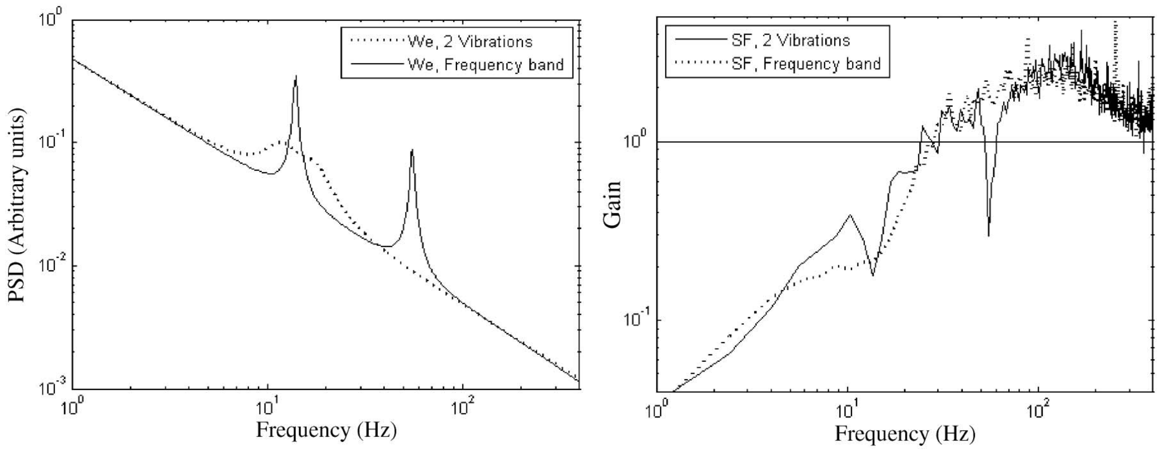

Fig. 18. Examples of H_∞ controllers for higher-order disturbances. Left: weighting functions modeling the disturbances; Right: resulting SFs in each case.

Unfortunately, this is not true for other disturbances, such as wind generated vibrations, where strong variations in their spectrum parameters can occur in time and also for different telescope orientations, deteriorating the overall performance of the system due to the associated model mismatches. This suggests the need for more sophisticated on-line identification techniques to provide the best rejection possible as the characteristics of the turbulence and disturbances change [23]. An example of the effect of these model discrepancies is the excessive rejection obtained in Fig. 17 (right) for the frequency of interest due to an erroneous identification of the vibration strength. According to Bode's theorem, such an unnecessary rejection is limiting the correction at other frequencies. Another problem associated to an incorrect turbulence modeling is the negative impact of an erroneous identification of the vibration frequency. We illustrate this effect in Fig. 19, where we show the residuals around a vibration peak, when the input vibration frequency varies by few Hz. Minor differences in frequency (a few hertz) cause the closed-loop response to behave substantially worse.

The principal benefit in the use of sophisticated controllers is that their SF is shaped to tackle specific frequencies where disturbances are concentrated and they lower the controller gain in other parts of the spectrum. A balanced or nearly flat spectrum of residuals would be expected in this optimal case, and although the theory behind Kalman and H_∞ controllers ensures this, the actual results tend to miss expectations. This is mainly due to inaccurate modeling of disturbances, nonlinearities, or dynamics present in the loop and not modeled (e.g., mirror dynamics). This suggests that the approach of relying on accurate identification tools for finding the turbulence and vibration parameters to tune the controllers might not be the right choice. We think that an approach that finely tunes the controllers looking for the lowest and balanced PSD of the measured residuals on a regular basis should be investigated. Another important finding is that the perturbations measured at a WFS level may be different from what actually appears on the science path, and the content may also evolve independently in one path from another. Having a way to measure the vibrations at the science detector level is then primordial to efficiently tackle these perturbations, and to perform the on-line optimization of the controllers.

Performance robustness can also be an issue in advanced controllers. We have found that uncertainties in the model can cause unacceptable closed-loop behavior that can even lead to instability. Parameter variations such as subaperture centroid gains or TTM dynamics not considered in the model can generate these undesirable dynamics. Using the same open-loop data from Fig. 11, simulations were run to determine the performance deterioration when a Kalman controller is designed based on the erroneous assumption of negligible TTM dynamics. Figure 20 shows three cases of actual TTM bandwidths: no dynamics (infinite bandwidth), 400 Hz (GeMS TTM bandwidth), and a fictitious 200 Hz bandwidth. In the second case (400 Hz, dashed line), the SF presents only a minor departure from the nominal curve. This was actually confirmed during the above implementation of the Kalman filter, where no significant deterioration in performance was found for this case. However, for a lower bandwidth of 200 Hz, the simulation results show an important loss in performance; this would lead to unacceptable oscillatory responses and noise amplification (dotted line). Solutions exist to include this dynamic during the design stage for both Kalman and H_∞ controllers. In the latter case, these dynamics can be included in the weighting function W_u and for the Kalman filter a solution can be implemented based on [21].

Due to Bode's theorem, the two controllers can always be shaped to generate similar performances, and both approaches reject the vibration frequency effectively, so the overall residual indices improve significantly when compared to the classical integrator. However, from the user's point of view, some

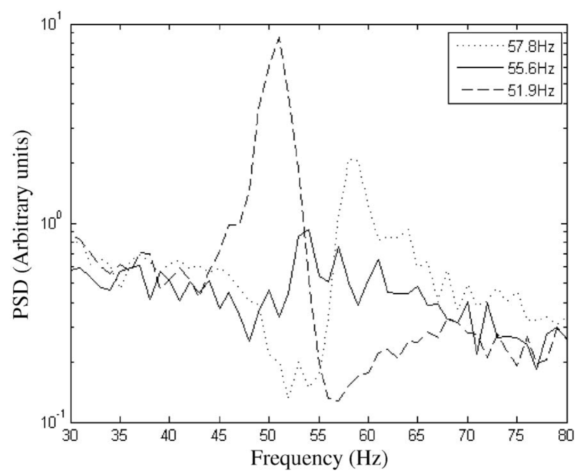

Fig. 19. Effect of frequency mismatch between real and modeled vibration frequencies. The continuous line corresponds to a correctly identified frequency. Departure from the correct frequency can degrade the performance.

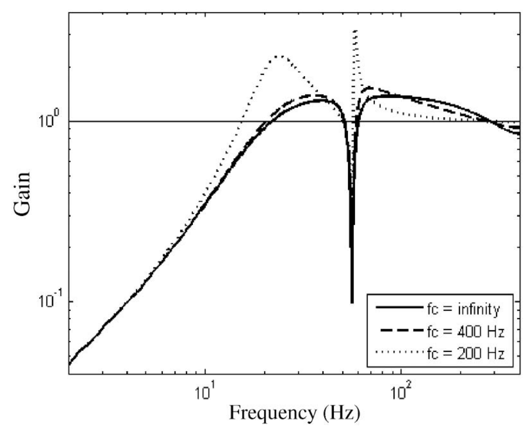

Fig. 20. Kalman SF under TTM bandwidth uncertainty.

Table 3. Summary of Controller Characteristics

Pros	Cons
Integrator	
- Highly robust - Very low computational demand - Simple to implement - Good rejection of low frequency turbulence	- Poor adaptivity to turbulence or disturbance conditions - No rejection of vibrations. It can amplify them for certain frequencies - Poor rejection of high frequency turbulence/ disturbances
Kalman	
- Excellent rejection of vibrations - Good rejection of low frequency turbulence - Simple implementation of the estimation process. - Simple and efficient implementation (sparse matrices)	- Low flexibility in disturbance modeling other than using AR2 - Including mirror dynamics increases complexity - Poor closed-loop stability for changes in the loop gain or dynamics - Rejection of vibrations deteriorates performance at other frequencies
H_∞	
- Excellent rejection of vibrations - Good rejection of low frequency turbulence - Flexible and intuitive modeling of disturbance and mirror dynamics (frequency framework used) - Optimal solution to estimation and control problems (solved comprehensively) - Optimization can be done using a quadratic or "worst case" approach (H_2 or H_∞) - Model reduction techniques proved effective and robust for high-order controllers	- Complex theory, although it basically requires the solution of 2 Ricatti equations - Use full matrices so higher computational demands - The order of the controller is determined by the dynamics of disturbances and mirror - Rejection of vibrations deteriorates performance at other frequencies

important differences exist in terms of implementation. Table 3 summarizes the advantages and disadvantages found during implementation and testing of these controllers.

7. Conclusions

The vibrational characteristics of the Gemini South telescope were determined experimentally using on-sky data from the GeMS and GSAOI instruments. Vibrational modes were found to exist at 14, 55, and 100 Hz. We have developed and tested three AO controllers to subdue these vibrations, although the suppression frequency can be adjusted simply by changing a parameter. The controllers were a standard integrator and the Kalman and H_∞ controllers. Experiments were performed on the GeMS bench using a Kolmogorov turbulence simulator and the TTM to artificially induce vibrations at the same frequencies as stated above. The residual slopes from the GeMS WFSs were used to estimate the performance. We find that substantial gain in performance can be achieved with advanced controllers when they are properly designed. In the case of large model errors, we found that the gain in performance provided by the advanced controllers is lost, showing similar results to the classical integrator.

This emphasizes the need for on-line identification and tuning procedures that would ensure optimality in performance. We think that together with classical identification tools, the flatness of the residual could be used as an optimization index to tune the controllers. This assumption is supported by two facts:

(i) In spite of identifying the disturbance models correctly, we found that very often the residual PSD differs from the expected flat response. This is probably due not only to varying characteristics of the disturbance, but also to unmodeled dynamics or nonlinearities in the AO system.

(ii) According to Bode's theorem and H_2/H_∞ theory, imbalances in the resulting closed-loop residual spectrum will take the performance away from the optimum; i.e., over-rejected frequencies will generate a worsening in performance in other parts of the spectrum and vice versa.

Finally, it is also interesting that no major differences were found in terms of performance between Kalman and H_∞; however, implementation and complexity issues are quite distinctive in each case, as summarized in Table 3.

This work has been supported by the Chilean Research Council (CONICYT) through grants Fondecyt 1095153 and Anillo ACT-86.

References

1. Y. Clenet, M. Kasper, N. Ageorges, C. Lidman, T. Fusco, O. P. Marco, M. Hartung, D. Mouillet, B. Koehler, G. Rousset, and N. Hubin, "NAOS performances: impact of the telescope vibrations and possible origins," in *Semaine de l'Astrophysique Francaise* (EdP Sciences, 2004), p. 179.
2. J. Maly, E. Darren, and T. Pargett, "Vibration suppression for the Gemini planet image," Proc. SPIE **7733**, 77331F (2010).
3. Y. Clenet, M. Kasper, N. Ageorges, C. Lidman, T. Fusco, G. Rousset, O. Marco, M. Hartung, D. Mouillet, B. Koehler, and N. Hubin, "NACO performance: status after 2 years of operation," Proc. SPIE **5490**, 107–117 (2004).

4. J. P. Verán and L. Poyneer, "Evaluation of the T/T conditions at Gemini South using NICI AO telemetry data," in *First AO4ELT Conference* (EdP Sciences, 2009), p. 05002.
5. J. Christou, C. Trujillo, B. Neichel, F. Rigaut, B. Walls, D. Coulson, J. White, A. Stephens, and M. Sheehan, "The effect of the instrument environment on the Altair AO system," presented at Second AO4ELT Conference, Victoria, British Columbia, Canada, 25–30 Sept. 2011.
6. C. Petit, J.-M. Conan, C. Kulcsár, and H. F. Raynaud, "Linear quadratic Gaussian control for adaptive optics and multiconjugate adaptive optics: experimental and numerical analysis," J. Opt. Soc. Am. A **26**, 1307–1325 (2009).
7. C. Petit, J. M. Conan, T. Fusco, J. Montri, C. Kulcsár, H. F. Raynaud, and D. Rabaud, "First laboratory demonstration of closed-loop Kalman based optimal control for vibration filtering and simplified MCAO," Proc. SPIE **6272**, 62721T (2006).
8. B. Neichel, F. Rigaut, A. Guesalaga, I. Rodriguez, and D. Guzman, "Kalman and H-infinity controllers for GeMS," in *Imaging Systems Applications* OSA Technical Digest (CD) (Optical Society of America, 2011), paper JWA32.
9. G. Agapito, F. Quirós-Pacheco, P. Tesi, A. Riccardi, and S. Esposito, "Observer-based control techniques for the LBT adaptive optics under telescope vibrations," Eur. J. Control **17**, 316–326 (2011).
10. J. M. Conan, H. F. Raynaud, C. Kulcsár, and S. Meimon, "Are integral controllers adapted to the new era of ELT adaptive optics?" presented at Second AO4ELT Conference, Victoria, British Columbia, Canada, 25–30 Sept. 2011.
11. E. Fedrigo, R. Muradore, and D. Zilio, "High performance adaptive optics system with fine tip/tilt control," Contr. Eng. Pract. **17**, 122–135 (2009).
12. B. Le Roux, J. M. Conan, C. Kulcsár, H. F. Raynaud, L. M. Mugnier, and T. Fusco, "Optimal control law for classical and multiconjugate adaptative optics," J. Opt. Soc. Am. A **21**, 1261–1276 (2004).
13. C. Kulcsár, H.-F. Raynaud, C. Petit, J.-M. Conan, and P. Viaris de Lesegno, "Optimal control, observers and integrators in adaptive optics," Opt. Express **14**, 7464–7476 (2006).
14. J. C. Doyle, K. Glover, P. P. Khargonekar, and B. A. Francis, "State-space solutions to standard H_2 and H_∞ control problems," IEEE Trans. Autom. Contr. **34**, 831–847 (1989).
15. M. G. Safonov, D. J. N. Limebeer, and R. Y. Chiang, "Simplifying the H_∞ theory via loop shifting, matrix pencil and descriptor concepts," Int. J. Contr. **50**, 2467–2488 (1989).
16. B. Bamieh and J. B. Pearson, "A general framework for linear periodic systems with application to H_∞ sampled-data control," IEEE Trans. Autom. Contr. **37**, 418–435 (1992).
17. B. L. Ellerbroek and F. Rigaut, "Methods for correcting tilt anisoplanatism in laser-guide-star-based multiconjugate adaptive optics," J. Opt. Soc. Am. A **18**, 2539–2547 (2001).
18. B. Neichel, F. Rigaut, M. Bec, M. Boccas, F. Daruich, C. D'Orgeville, V. Fesquet, R. Galvez, A. Garcia-Rissmann, G. Gausachs, M. Lombini, G. Perez, G. Trancho, V. Upadhya, and T. Vucina, "The Gemini MCAO systems GeMS: nearing the end of a lab-story," Proc. SPIE **7736**, 773606 (2010).
19. F. Rigaut and B. Neichel, "Gemini South MCAO on-sky results," presented at Second AO4ELT Conference, Victoria, British Columbia, Canada, 25–30 Sept. 2011.
20. J. M. Conan, G. Rousset, and P. Y. Madec, "Wave-front temporal spectra in high-resolution imaging through turbulence," J. Opt. Soc. Am. A **12**, 1559–1570 (1995).
21. E. Gendron and P. Lena, "Astronomical adaptive optics I. modal control optimization," Astron. Astrophys. **291**, 337–347 (1994).
22. C. Correia, H. F. Raynaud, C. Kulcsár, and J. M. Conan, "On the optimal reconstruction and control of adaptive optical systems with mirror dynamics," J. Opt. Soc. Am. A **27**, 333–349 (2010).
23. S. Meimon, C. Petit, T. Fusco, and C. Kulcsár, "Tip–tilt disturbance model identification for Kalman-based control scheme: application to XAO and ELT systems," J. Opt. Soc. Am. A **27**, A122–A132 (2010).
24. C. Dessenne, P.-Y. Madec, and G. Rousset, "Modal prediction for closed-loop adaptive optics," Opt. Lett. **22**, 1535–1537 (1997).
25. C. Mohtadi, "Bode's integral theorem for discrete-time systems," IEE Proc. D Contr. Theory Appl. **137**, 57–66 (1990).